CHEMISTRY
A EUROPEAN JOURNAL

DOI: 10.1002/chem.200800227

VIP

# Studies of Finite Molecular Chains: Synthesis, Structural, Magnetic and Inelastic Neutron Scattering Studies of Hexa- and Heptanuclear Chromium Horseshoes

**Stefan T. Ochsenbein,[b] Floriana Tuna,[a] Marzio Rancan,[a] Rachel S. G. Davies,[a] Christopher A. Muryn,[a] Oliver Waldmann,[b] Roland Bircher,[b] Andreas Sieber,[b] Graham Carver,[b] Hannu Mutka,[c] Felix Fernandez-Alonso,[d] Andrew Podlesnyak,[e] Larry P. Engelhardt,[f] Grigore A. Timco,[a] Hans U. Güdel,*[b] and Richard E. P. Winpenny*[a]**

*Dedicated to Professor Jan Reedijk on the occasion of his 65th birthday and his retirement*

**Abstract:** We report the synthesis and structural characterisation of a family of finite molecular chains, specifically $[\{[R_2NH_2]_3[Cr_6F_{11}(O_2CCMe_3)_{10}]\}_2]$ (in which R = *n*Pr **1**, Et **2**, *n*Bu **3**), $[\{Et_2NH\}_2\{[Et_2NH_2]_3[Cr_7F_{12}(O_2CCMe_3)_{12}][HO_2CCMe_3]_2\}_2]$ (**4**), $[\{[Me_2NH_2]_3[Cr_6F_{11}(O_2CCMe_3)_{10}]\cdot 2.5\,H_2O\}_4]$ (**5**) and $[\{[iPr_2NH_2]_3[Cr_7F_{12}(O_2CCMe_3)_{12}]\}_2]$ (**6**). The structures all contain horseshoes of chromium centres, with each Cr···Cr contact within the horseshoe bridged by a fluoride and two pivalates. The horseshoes are linked through hydrogen bonds to the secondary ammonium cations in the structure, leading to di- and tetra-horseshoe structures. Through magnetic measurements and inelastic neutron scattering studies we have determined the exchange coupling constants in **1** and **6**. In **1** it is possible to distinguish two exchange interactions, $J_A = -1.1$ meV and $J_B = -1.4$ meV; $J_A$ is the exchange interactions at the tips of the horseshoe and $J_B$ is the exchange within the body of the horseshoe (1 meV = 8.066 $cm^{-1}$). For **6** only one interaction was needed to model the data: $J = -1.18$ meV. The single-ion anisotropy parameters for $Cr^{III}$ were also derived for the two compounds as: for **1**, $D_{Cr} = -0.028$ meV and $|E_{Cr}| = 0.005$ meV; for **6**, $D_{Cr} = -0.031$ meV. Magnetic-field-dependent inelastic neutron scattering experiments on **1** allowed the Zeeman splitting of the first two excited states and level crossings to be observed. For the tetramer of horseshoes (**5**), quantum Monte Carlo calculations were used to fit the magnetic susceptibility behaviour, giving two exchange interactions within the horseshoe (−1.32 and −1.65 meV) and a weak inter-horseshoe coupling of +0.12 meV. Multi-frequency variable-temperature EPR studies on **1**, **2** and **6** have also been performed, allowing further characterisation of the spin Hamiltonian parameters of these chains.

**Keywords:** chain complexes · chromium · EPR spectroscopy · magnetic measurements · neutron scattering

[a] Dr. F. Tuna, M. Rancan, R. S. G. Davies, Dr. C. A. Muryn, Dr. G. A. Timco, Prof. R. E. P. Winpenny
School of Chemistry, The University of Manchester
Oxford Road, Manchester M13 9PL (UK)
Fax: (+44) 161-275-4616
E-mail: richard.winpenny@man.ac.uk

[b] Dr. S. T. Ochsenbein, Dr. O. Waldmann, Dr. R. Bircher, Dr. A. Sieber, Dr. G. Carver, Prof. Dr. H. U. Güdel
Department of Chemistry and Biochemistry
University of Bern, Freiestrasse 3, 3000 Bern 9 (Switzerland)
Fax: (+41) 31-631-43-99
E-mail: hans-ulrich.guedel@iac.unibe.ch

[c] Dr. H. Mutka
Institut Laue-Langevin, 6 Rue Jules Horowitz
BP 156-38042, Grenoble Cedex 9 (France)

[d] Dr. F. Fernandez-Alonso
ISIS Facility, CCLRC Rutherford Appleton Laboratory
Chilton, Didcot OX11 0QX (UK)

[e] Dr. A. Podlesnyak
Laboratory for Neutron Scattering
ETH Zürich and PSI Villigen, 5232 Villigen PSI (Switzerland)

[f] Dr. L. P. Engelhardt
Department of Physics and Astronomy
Francis Marion University, Florence, South Carolina (USA)

## Introduction

Two classes of molecules have been heavily studied in the field of spin clusters in recent years. Most work has been done on "single-molecule magnets" (SMMs),[1–4] which are high-spin molecules that retain magnetisation in the absence of a magnetic field due to anisotropy of the spin ground state. Secondly there has been much work on antiferromagnetically coupled (AFM) wheels.[5–14] AFM wheels are aesthetically pleasing and allow detailed investigation of quantum phenomena.[9,13,15–17] It has also been proposed that heterometallic AFM wheels that possess an $S=1/2$ ground state could be used in quantum information processing.[9,18–20]

Much rarer than the AFM wheels are finite AFM chains. There are an interesting family of such chains involving Ni[21] Cr[22] and Co centres[23] bridged by oligo-α-dipyridylamines; in these chains the magnetic exchange is normally very strong. Another family of finite chains can be made by adapting the synthetic procedure that generates the heterometallic AFM wheels.[9,24] Here we discuss studies of hexa- and heptanuclear finite molecular chains.

Our detailed investigation of the magnetism in these chains, by magnetisation measurements, inelastic neutron scattering (INS) and electron paramagnetic resonance spectroscopy (EPR), was motivated by the large interest in understanding the physical nature of the magnetic ground states and excitations in molecular spin clusters.[13] In most clusters the Heisenberg interactions between the metal centres are the dominant terms, raising the general question of the possible magnetic phenomena due to Heisenberg interactions, which is evidently very fundamental. The answers, however, would also be relevant to chemistry, as they may suggest strategies for synthesising new topologies of potential interest or even compounds with desired magnetic properties.

The AFM wheels have become prototypical systems in this regard, and allow an important general insight into the problem of which ground states and spin excitations may emerge from Heisenberg interactions. In particular, they suggest what may be called the "L&E-band picture",[13,15,25] which appears to be generic for a rather large class of Heisenberg spin clusters. In this picture, the low-lying energy spectrum consists of several rotational bands, those energies increase according to the Landé pattern $E(S)\propto S(S+1)$. The lowest band, the L-band, corresponds to a (quantised) rotation of the Néel vector,[13,15,25–29] and the next higher ones, collectively called the E-band, may be pictured as (discrete) AFM spin waves.[13,15,25,26]

Studying AFM chains in this context, and comparing them to AFM wheels, is highly desirable, as it will be interesting to see the characteristic effects due to the change of the boundary conditions from periodic (wheels) to open (chains). The physical nature of the excitations and spin structure in the hexanuclear chain was discussed recently.[30] We here present a brief review of the L&E-band concept with a discussion of the finite chains in particular, including a chemical analogy for the excitations observed in the hexanuclear chain, which may help chemists to better understand some key aspects of the magnetic excitations in Heisenberg spin clusters.

## Results and Analysis

**Synthesis and structural studies**: The horseshoes (**1**–**6**) are all made by the same procedure, which is the reaction of hydrated chromium fluoride with pivalic acid in the presence of a secondary amine. In the absence of this amine the parent molecule, the homometallic $[\{CrF(O_2CCMe_3)_2\}_8]$ wheel (**7**) forms.[12] This compound is also a by-product of the reactions that produce the horseshoes if a small amount of a secondary amine is used in reaction, or if heating is to a higher temperature or for a longer period of time. Our belief is that it is hydrogen bonding between the fluoride ions and the protonated amines that slows the formation of **7**; the protonated amines stabilise the finite chains, which can then be crystallised by careful choice of conditions. We have examined a range of secondary amines to see if different chains can be stabilised in different reaction conditions.

With di-*n*-propyl- and di-*n*-butylamine the only horseshoe products we have crystallised are $[\{[nPr_2NH_2]_3[Cr_6F_{11}(O_2CCMe_3)_{10}]\}_2]$ (**1**) and $[\{[nBu_2NH_2]_3[Cr_6F_{11}(O_2CCMe_3)_{10}]\}_2]$ (**3**). The structure of **1** is shown in Figure 1. The individual

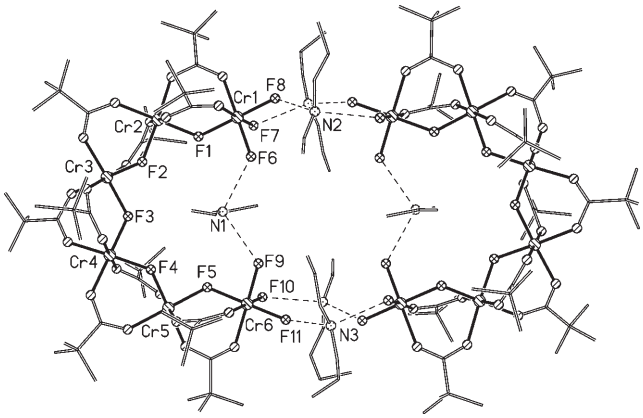


Figure 1. The structure of **1** in the crystal.

$\{Cr_6\}$ cages have the shape of a horseshoe, with each Cr···Cr edge bridged by a fluoride and two pivalates. The $Cr^{III}$ ions at the tips of the horseshoe (Cr1 and Cr6) each have four fluorides (of which three terminal) and two carboxylates coordinated, while the other $Cr^{III}$ ions each have two fluorides and four carboxylates coordinated. The structure is clearly related to **7**, and to the heterometallic rings, missing two metal centres to complete a wheel.

In **1** and **3** the horseshoes are arranged in pairs related by inversion symmetry in the crystal structure. A secondary ammonium cation is within each horseshoe, in an analogous position to the templating ammonium ions in the heterometallic wheels. These ammonium cations form hydrogen

  

bonds to terminal fluorides. In both structures four further secondary ammonium cations are located between the tips of the horseshoes and also form hydrogen bonds to terminal fluorides. Therefore, a pseudo-macrocycle containing twelve $Cr^{III}$ ions is formed.

For shorter secondary amines a more varied picture is found. When $Et_2NH$ is used an analogous structure to **1** and **3** can be formed in the same conditions. $[\{[Et_2NH_2]_3[Cr_6F_{11}(O_2CCMe_3)_{10}]\}_2]$ (**2**) has an identical arrangement of horseshoes and ammonium cations as in **1**. However when half as many mole equivalents of $Et_2NH$ is used a mixture of compounds is formed. The major product is **2**, which was extracted in $Et_2O$ with some trace of $[\{CrF(O_2CCMe_3)_2\}_8]$ (detected by EI MS and TLC). A small amount of a further product remains ($\approx$100 mg) which is less soluble in $Et_2O$. This product was extracted with THF, filtered and the THF removed by evaporation prior to crystallisation from pentane/acetone. A very small amount of two different shaped crystals were obtained. These were identified by X-ray crystallography as $[\{Et_2NH\}_2\{[Et_2NH_2]_3[Cr_7F_{12}(O_2CCMe_3)_{12}][HO_2CCMe_3]_2\}_2]$ (**4**) and $[\{[Et_2NH_2]_3[Cr_7F_{10}(O_2CCMe_3)_{14}]\}_2]$ (**4a**). The structure of **4a** is of insufficient quality to report; however, it appears to contain a similar structure to **4** but with terminal fluorides replaced by pivalate ligands.

The structure of **4** (Figure 2) contains a dimer of horseshoes, but contains $\{Cr_7\}$ horseshoes rather than hexanuclear

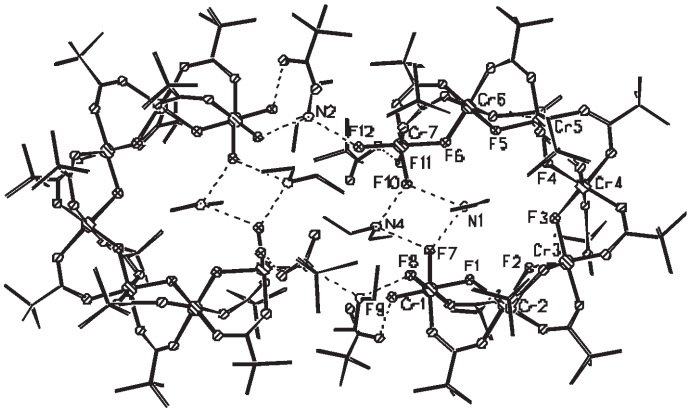


Figure 2. The structure of **4** in the crystal.

chains. The Cr···Cr vectors are bridged as in **1**–**3**, and again there are three terminal fluorides on the $Cr^{III}$ sites at the tips of the horseshoe.

As in **1**–**3** there are hydrogen bonds from each horseshoe to a central ammonium cation (N1), but the arrangement of the four further ammonium cations is quite different. Two (the ammonium containing N4 and the symmetry equivalent) form hydrogen bonds to terminal fluorides from the same horseshoe (e.g., F7 and F10 in Figure 2). The final two (N2 and the symmetry equivalent) form hydrogen bonds to fluorides from different horseshoes (e.g., F12 and F8A or F8 and F12A). Therefore compared with **1**–**3** we have only two fluorides linking the horseshoes rather than four. The two horseshoes in **4** are not co-planar, with a step at the bridging ammoniums.

The remaining terminal fluorides (F9 and F11) are involved in hydrogen bonding to pivalic acid molecules. A further $Et_2NH$ group is found in the lattice, which is not involved in hydrogen-bonding interactions.

If $Me_2NH$ is used as the secondary amine the resulting structure is more complex. In place of the dimer of horseshoes we find a hydrogen-bonded tetramer, $[\{[Me_2NH_2]_3[Cr_6F_{11}(O_2CCMe_3)_{10}]\cdot 2.5H_2O\}_4]$ (**5**; Figure 3). The individual

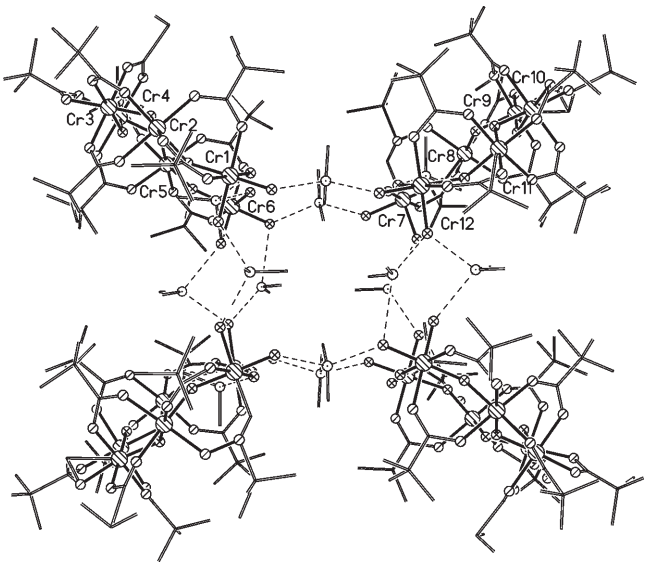


Figure 3. The structure of the "cross of horseshoes" of **5** in the crystal.

$\{Cr_6\}$ horseshoes are analogous to those found in **1**–**3**, and each has a $[Me_2NH_2]^+$ ion within each horseshoe. However the horseshoes pack with hydrogen bonds to eight further $[Me_2NH_2]^+$ ions with $\{Cr_6\}$ horseshoes arranged in a cross (Figure 3).

If $iPr_2NH$ is used as the secondary amine a fourth structural type is found. $[\{[iPr_2NH_2]_3[Cr_7F_{12}(O_2CCMe_3)_{12}]\}_2]$ (**6**) contains $\{Cr_7\}$ horseshoes similar to that in **4**, but with hydrogen bonding between the horseshoes similar to that found in the structures of **1**–**3** (Figure 4), that is, there is an ammonium cation at the centre of each horseshoe, and four further $iPr_2NH_2$ cations hydrogen bonding between the $\{Cr_7\}$ chains. All the fourteen Cr centres lie in the same plane.

**Magnetic measurements of 1, 2, 5 and 6**: Physical studies have been pursued on four representative examples: three dimers of horseshoes, **1, 2** and **6**, and also the tetramer of horseshoes, **5**.

The magnetic susceptibility ($\chi$) versus temperature of **1** is shown in Figure 5. It exhibits two maxima at about 4 and 16 K, indicative of AFM interactions. Observation of two maxima is unusual; such a feature has been reported previously for the AFM wheel $\{Cr_8Ni\}$[31] and in $\{Cr_{10}Cu_2\}$ rings.[32]

  

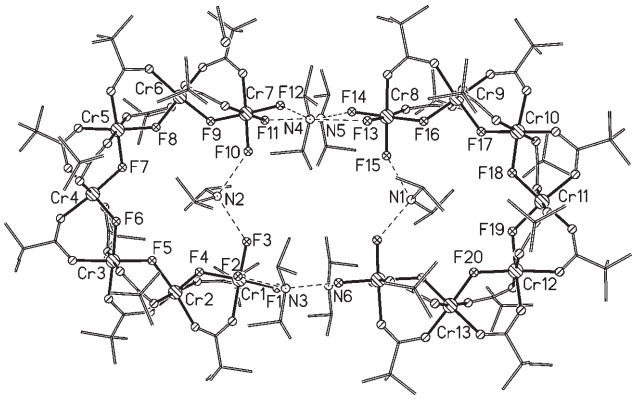


Figure 4. The structure of **6** in the crystal

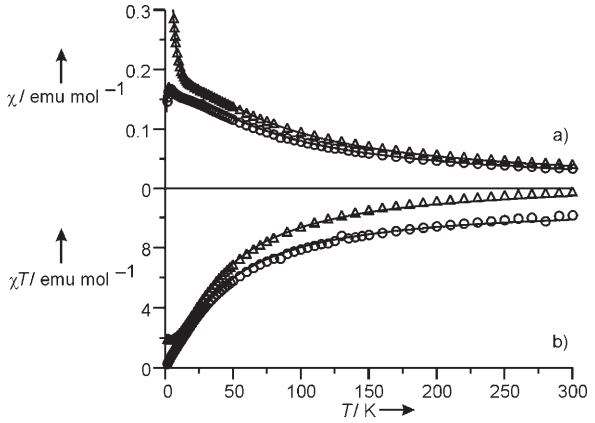


Figure 5. The molar magnetic susceptibility of **1** (○) and **6** (△) plotted as a) $\chi$ and b) $\chi T$ versus temperature measured at 0.1 T. The solid lines are calculated curves with parameters given in the text.

The $\chi T$ value of 9.84 emu K mol$^{-1}$ at 300 K is somewhat smaller than the calculated value of 11.02 emu K mol$^{-1}$ for six uncoupled $Cr^{III}$ ions with $S_j=3/2$ and $g=1.98$, indicating AFM interactions between the $Cr^{III}$ ions. Towards the lowest temperature $\chi T$ approaches zero, suggesting a spin ground state of $S=0$, consistent with the even number of $Cr^{III}$ ions and AFM interactions. Compound **2** shows similar behaviour.

The magnetic behaviour of **1** and **2** can be described by the spin Hamiltonian given in Equation (1) in which $J_A$ represents the Heisenberg exchange between Cr1 and Cr2, and between Cr5 and Cr6, that is, the couplings at the tips of the horseshoe; $J_B$ is the exchange coupling between the remaining $Cr^{III}$ ions; $D_{Cr}$ is the axial and $E_{Cr}$ the rhombic zero-field splitting (ZFS) parameter of the $Cr^{III}$ ions.

$$\mathscr{H} = -J_A(\hat{\mathbf{S}}_1\hat{\mathbf{S}}_2 + \hat{\mathbf{S}}_5\hat{\mathbf{S}}_6) - J_B(\hat{\mathbf{S}}_2\hat{\mathbf{S}}_3 + \hat{\mathbf{S}}_3\hat{\mathbf{S}}_4 + \hat{\mathbf{S}}_4\hat{\mathbf{S}}_5) + D_{Cr}\sum_{j=1}^{6}\hat{S}_{j,z}^2 + E_{Cr}\sum_{j=1}^{6}(\hat{S}_{j,x}^2 + \hat{S}_{j,y}^2) \quad (1)$$

The magnetic behaviour of **1** can be modelled well (Figure 5) with $g=1.98$, $J_A=-1.16$ meV, $J_B=-1.40$ meV, while the best fit of data measured on **2** gives the parameters, $g=1.98$, $J_A=-1.14$ meV, $J_B=-1.48$ meV (1 meV = 8.066 cm$^{-1}$). The susceptibility data do not allow the ZFS parameters to be determined.

For **6**, the $\chi$ value increases slightly from 0.04 emu mol$^{-1}$ at 300 K to a broad local maximum at around 30 K (Figure 5). Below 15 K a steep increase is observed to 1.01 emu mol$^{-1}$ at 1.8 K. The $\chi T$ value decreases from 11.61 emu K mol$^{-1}$ at 300 K to a minimal value of 1.76 emu K mol$^{-1}$ at 4.0 K, before a slight increase to 1.83 emu K mol$^{-1}$ at 1.8 K occurs (Figure 5). The $\chi T$ value of 11.61 emu K mol$^{-1}$ at 300 K is below the calculated value of 12.86 emu K mol$^{-1}$ for seven uncoupled $Cr^{III}$ ions with $S=3/2$ and $g=1.98$, indicating that the AFM interactions affect the susceptibility up to 300 K. The subsequent decrease of $\chi T$ with decreasing temperature is a further sign of AFM interactions. The low-temperature $\chi T$ value of 1.83 emu K mol$^{-1}$ is in good agreement with the calculated value of 1.84 emu K mol$^{-1}$ expected for a spin ground state of $S=3/2$ and $g=1.98$. The field dependence of the magnetisation measured at 1.8 K is depicted in Figure 6. It shows a typical saturation

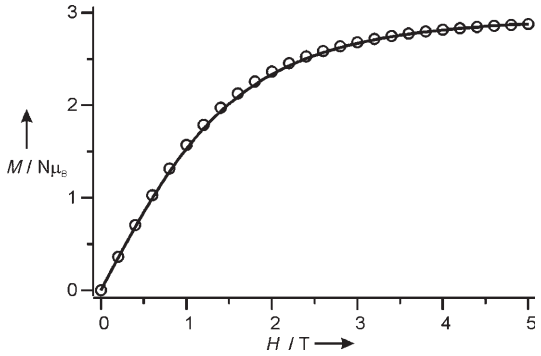


Figure 6. Field-dependence of the magnetisation of **6** measured at 1.8 K. The solid line is a calculation with $S=3/2$, $D_{3/2}=-0.045$ meV, and $g=1.96$.

behaviour, and at 5 T a value of 2.88 $N_A\mu_B$ near saturation. This is in good agreement with an $S=3/2$ ground state.

The magnetic susceptibility data can be modelled by using a similar spin Hamiltonian to that in Equation (1), again neglecting anisotropy, but with an additional Cr spin centre included. For **6** only a single Cr···Cr exchange interaction of −1.18 meV was required for a good fit of the susceptibility data. There is also no need to include magnetic interactions between the paramagnetic individual horseshoes to fit the susceptibility behaviour.

For **5**, the $\chi$ values increases gradually across the entire temperature range, with a very sharp increase below 20 K (Figure 7). The $\chi T$ value of 39.3 emu K mol$^{-1}$ at room temperature is a little below that calculated for 24 $Cr^{III}$ centres (44.1 emu K mol$^{-1}$ for $g=1.98$) and decreases smoothly with decreasing temperature. This is sign of antiferromagnetic exchange between the metal centres. At the lowest tempera-

  

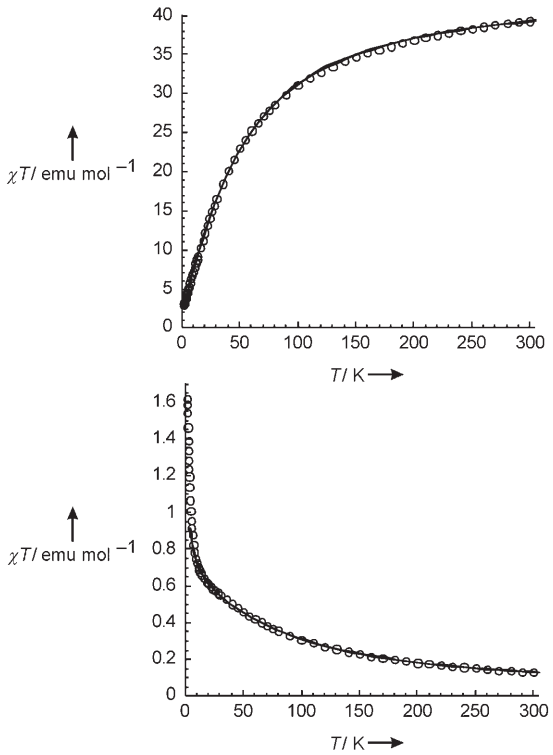


Figure 7. The molar magnetic susceptibility of **5** plotted as $\chi T$ against $T$ (top) and $\chi$ against $T$ (bottom). The solid line is a curve calculated using quantum Monte Carlo procedures and the parameters given in the text.

ture we have measured $\chi T$ is still falling rapidly. The temperature dependence of $\chi$ for **5** is markedly different to that observed for **1**, which contains the same $\{Cr_6\}$ repeat unit. Specifically, the point at which $\chi$ reaches a maximum for **1** and then falls, $\chi$ for **5** is still rising at the lowest temperatures measured.

This residual paramagnetism of **5** at very low temperature can be explained in several ways. Such paramagnetism could be the result of a paramagnetic ground state for each horseshoe—which seems unlikely given the results for **1.** Alternatively the explanation could be the presence of low-lying paramagnetic excited states of the supramolecular tetramer, as we have found previously for heterometallic rings.[31,32] A third explanation—and one very commonly adopted in the magnetochemistry literature—is to assume that this low-temperature rise in $\chi$ is due to a paramagnetic impurity. This assumption—if unsupported by other evidence, for example, elemental analysis—allows a fit of data to be performed that may have no validity as it introduces an unjustified parameter, namely the percentage of paramagnetic impurity.

As all evidence is that **5** is a pure compound, the variable-temperature behaviour of susceptibility has been modelled by using quantum Monte Carlo (QMC) techniques.[32,33] The results are shown in Figure 7. The assumption was made that a weak interaction could exist between the horseshoes, presumably through hydrogen-bonding paths involving the bridging ammonium cations. The QMC treatment, which allows many possible sets of exchange parameters to be examined very quickly, leads to an excellent fit with parameters: $g=1.98$, $J_A=-1.32$, $J_B=-1.65$ and $J_C=+0.12$ meV (in which $J_A$ and $J_B$ have the same meaning as in the discussion above, and $J_C$ is the coupling between horseshoes). The low-temperature rise in $\chi$ can be modelled to 5 K, but below this temperature frustration effects make application of QMC difficult; the calculations do not converge. However the fit over the temperature range from 300–5 K, and the clear indication of a rise in $\chi$ at low temperature suggests the model is good. The exchange parameters are in broad agreement with those calculated for **1** and **2**, and with those used to fit INS data of **1** (see below).

**Zero-field inelastic neutron scattering (INS) of 1**: INS spectra of **1** at 1.6, 9.5 and 20 K were obtained on an IN5 instrument with an initial neutron wavelength of $\lambda_i=3.8$ Å (Figure 8a). The high sloping background is ascribed to a non-magnetic origin due to the hydrogen content of the sample, while the sharper peaks are assigned to magnetic excitations. We applied the so-called Bose correction to subtract the background due to hydrogen atoms. The 20 K data were divided by the Bose population factor for phonons[34] at 20 K and then multiplied with the population factor for 9.5 or 1.6 K. The resulting Bose corrected intensity was then subtracted from the 9.5 and 1.6 K data. In this way the spectra in Figure 8b were obtained, which confirms that the sloping background in the raw data was due to phonons.

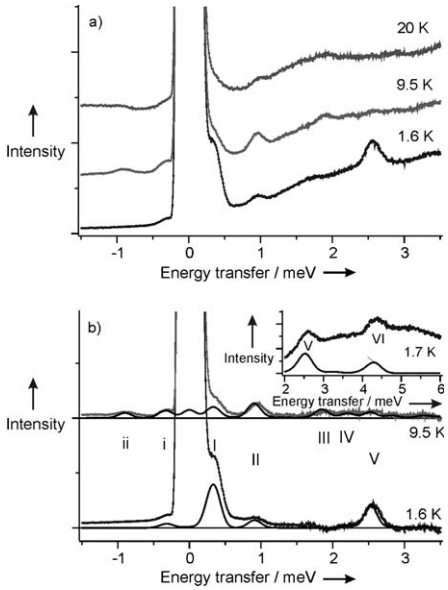


Figure 8. a)INS spectra of **1** obtained on IN5 (ILL) with an incoming neutron wavelength $\lambda_i=3.8$ Å at 1.6, 9.5 and 20 K. Summed over all scattering angles. b) INS spectra of **1** after Bose correction. The inset shows part of a spectrum obtained with $\lambda_i=3.0$ Å at 1.7 K. The black solid lines are calculated spectra, with $J_A=-1.1$ meV, $J_B=-1.4$ meV, $D=-0.028$ meV, and $|E|=0.005$ meV.

Five peaks are observed, labelled I–V, on the neutron energy loss side, and two (I′ and II′) on the gain side. From

  

the temperature dependence it becomes clear that peak I at 0.32(1) meV and peak V at 2.55(1) meV are transitions from the ground state (cold transitions), while peaks II, III and IV at 0.93(2), 1.89(1), and 2.21(2) meV, respectively, are hot transitions. Peaks I′ and II′ on the energy gain side are the equivalents of transitions I and II on the loss side, and lie at −0.32(1) and −0.91(1) meV, respectively. The inset of Figure 8a shows a spectrum obtained with a wavelength of $\lambda_i$= 3.0 Å at 1.7 K. Peak V is observed at 2.6(1) meV, and a new peak VI at 4.4(1) meV. These data are not Bose corrected, as we have only measured at low temperature with $\lambda_i$= 3.0 Å.

The neutron energy loss side of the INS spectra of **1** at 1.5 and 10 K obtained on IRIS with final neutron wavelength $\lambda_f$=6.66 Å are depicted in Figure 9. The broad extension of

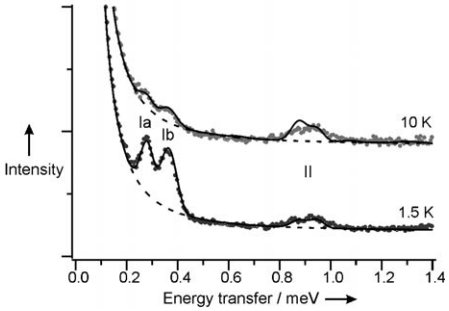


Figure 9. INS spectra of **1** obtained on IRIS with final wavelength $\lambda_f$= 6.66 Å. The dashed line accounts for thermal diffuse scattering, and the solid lines are calculated spectra with $J_A$=−1.1 meV, $J_B$=−1.4 meV, $D$= −0.028 meV, and $|E|$=0.005 meV.

the elastic line is due to thermal diffuse scattering. The spectra are characterised by a double peak at around 0.3 meV {Ia: 0.281(1) meV; Ib: 0.357(1) meV}, which loses intensity with increasing temperature (=cold transitions), and by a broad peak at 0.919(3) meV (II) with more intensity at 10 K than at 1.5 K (=hot transition).

The INS data can be reproduced with only one exchange coupling constant, $J_A=J_B=-1.27$ meV.[30] A significantly better fit, however, is obtained using two different exchange coupling constants that account for the different coordination environment that the $Cr^{III}$ ions at the tips of the horseshoe have compared to the other $Cr^{III}$ ions. This is also required to fit the magnetic susceptibility data adequately (see above).

Numerically diagonalising Equation (1) yields the energy eigenvalues $E_n$ and the corresponding wavefunctions $|n\rangle$. These can be used to calculate the INS intensity for a transition $i\rightarrow f$, which is proportional to the scattering function $S^{\alpha\beta}(\mathbf{Q},\omega)$ given in Equation (2),[35] in which $j,j'$ is the number of the $Cr^{III}$ centre; $\alpha$ and $\beta$ stand for Cartesian coordinates $x$, $y$, $z$; $\hat{S}_{j,\alpha}$ is the α component of the spin operator $\hat{\mathbf{S}}_j$ at position $\mathbf{r}_j$; $|i\rangle$ is the initial state of a transition with energy $E_i$; $|f\rangle$ the final state with energy $E_f$; $p_i$ is the Boltzmann population factor of state $|i\rangle$ and $\mathbf{Q}$ is the scattering vector or the momentum transfer between neutron and sample, respectively.

$$S^{\alpha\beta}(\mathbf{Q},\omega) = \sum_{jj'} \exp(i\mathbf{Q}(\mathbf{r}_j-\mathbf{r}_{j'}))\times \sum_{i,f} p_i\langle i|\hat{S}_{j,\alpha}|f\rangle\langle f|\hat{S}_{j',\beta}|i\rangle\delta(E_i-E_f+\hbar\omega) \quad (2)$$

For powder samples, Equation (2) has to be averaged in $\mathbf{Q}$ space using known formulae.[36,37] The $Q$ dependence of the INS intensity given by so-called interference factors of a certain transition bears information about the wavefunctions of the involved states.[36,38] Unfortunately, due to the incoherent scattering from the hydrogen atoms in our sample, the $Q$ dependence could not be evaluated. Therefore, we summed the spectra over all scattering angles, and hence over the whole $Q$ range. We calculated the INS intensities accordingly, assuming Gaussian line shapes with a full-width-half-maximum (FWHM) of 0.4 meV for the IN5 spectrum with $\lambda_i$=3.0 Å, 0.2 meV for the IN5 spectra with $\lambda_i$= 3.8 Å, and 0.03 meV for the IRIS spectra. We employed sparse matrix techniques with a homemade program to calculate the lowest states in energy,[25,37] because the calculation of all energies, wave functions and transition matrix elements as required for obtaining the INS intensity would be time-consuming with our present computing power (Hilbert space: 4096).

Excellent agreement between measured and calculated INS energies and intensities was obtained with the parameters $J_A=-1.1$ meV, $J_B=-1.4$ meV, $D_{Cr}=-0.028$ meV, and $|E_{Cr}|=0.005$ meV, shown as solid lines in Figures 8 and 9. The negative coupling constants give an $S=0$ ground state; the excited states have $S\neq0$, and the anisotropy parameters mean these states will undergo zero-field splitting, that is, not all $M_S$ states within a specific $S$ state will be degenerate. Because of the lower resolution, the ZFS is not observed in the IN5 data. The value of $D_{Cr}$ is unambiguously determined by the energy difference of peaks Ia and Ib in the high-resolution IRIS data; and $E_{Cr}$ by the intensities and a broadened linewidth of peak Ib.

Peaks I and V are transitions from the $S=0$ ground state to excited $S=1$ states. Peak V consists of two transitions, but the energies of the two $S=1$ states at approximately 2.5 meV are degenerate in our model. Peak VI contains three unresolved transitions from the ground state into $S=1$ states. Peak II corresponds to a transition from the lowest $S=1$ state to the lowest $S=2$ state, and peak III from this $S=2$ state to the lowest $S=3$ state. Transition IV is a transition between the second $S=1$ state and a higher excited $S=$ 2 state.

The lowest states of the calculated energy spectrum and the observed transitions are shown in Figure 10. As the anisotropy is smaller than the exchange interaction (strong-exchange limit), it is still possible to represent the wavefunctions in $|S,M_S\rangle$ notation, indicating the dominant contribution. The axial ZFS terms split the $S=1$ state into $|1,0\rangle$ and $|1,\pm1\rangle$, while the rhombic terms lead to a mixing of the

  

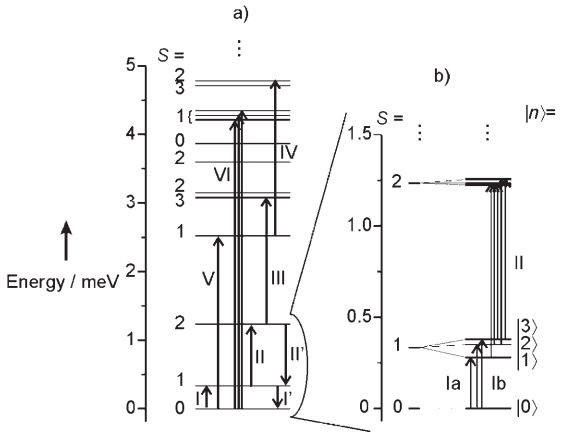


Figure 10. a) Calculated isotropic energy spectrum of **1** below 5 meV with $J_A=-1.1$ meV and $J_B=-1.4$ meV. b) Including anisotropy with $D=-0.028$ meV and $|E|=0.005$ meV.

wavefunctions of states differing by $\Delta M_S=\pm 2$. Hence it admixes $|1,+1\rangle$ and $|1,-1\rangle$, which leads to the splitting into $|2\rangle$ and $|3\rangle$ shown in Figure 10, and hence to the observed broadening of peak Ib in Figure 9. We cannot determine the sign of $E_{Cr}$ from this data.

The anisotropy splitting of the $S=2$ state is much smaller, and cannot be determined by INS; however it is resolved by EPR spectroscopy (see below). In addition peak II appears to consist of several transitions, due to the ZFS of the initial $S=1$ and final $S=2$ state. This accounts for the breadth of this peak.

**Zero-field inelastic neutron scattering (INS) of 6**: Figure 11 shows the neutron energy loss side of the INS spectra for **6** measured on IRIS at 1.5 and 10 K. The solid line in Figure 11a is an analytical function comprising a Gaussian and a Lorentzian, which accounts for the thermal diffuse scattering background. Subtraction of this background yields the spectra shown in Figure 11b. At 1.5 K three well resolved peaks at 0.09 (I), 0.63 (II) and 0.72 meV (III) are observed. Peaks I–III lose intensity with increasing temperature (=cold transitions), while a broader peak at 1.13 meV (IV) appears (=hot transition). Furthermore, at the upper edge of the spectra some intensity is observed. It is also associated with a magnetic transition (V); it is slightly less intense at 10 K than at 1.5 K.

In order to model the INS spectra of **6**, we used the Hamiltonian given in Equation (3), in which $J$ is the isotropic exchange constant between the $Cr^{III}$ ions in the chain and $D_{Cr}$ is the single-ion ZFS parameter.

$$\mathscr{H} = -J\sum_{j=1}^{6}\hat{\mathbf{S}}_j\hat{\mathbf{S}}_{j+1} + D_{Cr}\sum_{j=1}^{7}\hat{S}_{j,z}^2 \qquad (3)$$

As for **1** and the homo- and heterometallic $Cr^{III}$-containing wheels,[39,41] the AFM exchange coupling is expected to be the leading term. The resulting spin ground state is $S=$

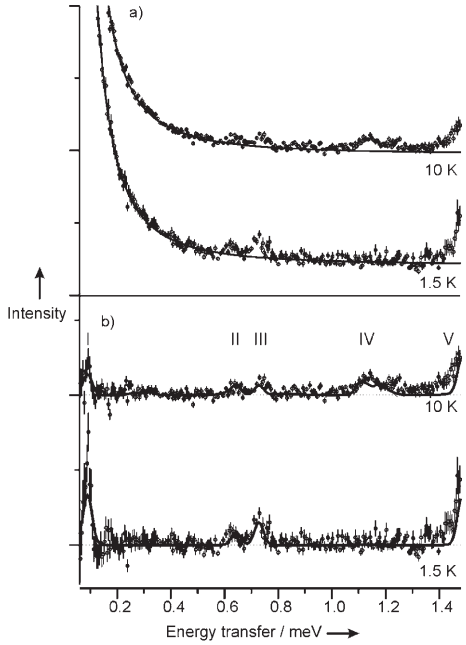


Figure 11. a) INS spectra of **6** measured at 1.5 and 10 K on the backscattering spectrometer IRIS with a final wavelength $\lambda_f=6.66$ Å. The solid lines are derived from an analytical function accounting for thermal diffuse background scattering. b) Measured spectra after background subtraction. The solid lines represent the simulated spectra for $J=-1.18$ meV, $D=-0.031$ meV, and FWHM = 0.03 meV.

3/2, which is zero-field split into the two Kramer's doublets $M_S=\pm 3/2$ and $M_S=\pm 1/2$. $D_{Cr}$ is expected to be negative in analogy to **1**, and the other $Cr^{III}$-containing wheels.[39,41] The analysis and calculation of the INS intensity was done as for **1** (for **6** the Hilbert space is 16384), and we assumed Gaussian line shapes with a FWHM of 0.03 meV. The best agreement between calculated and observed spectra was obtained for $J=-1.18$ meV and $D_{Cr}=-0.031$ meV, shown as solid lines in Figure 11b. A part of the calculated energy spectrum is shown in Figure 12, with energy states labelled again in

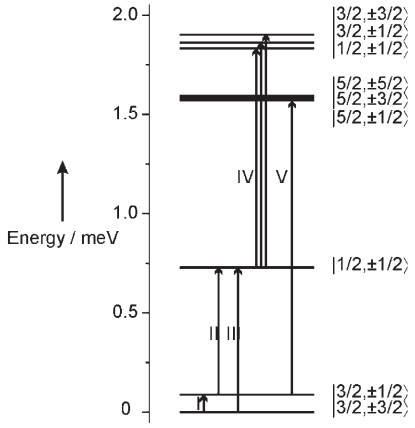


Figure 12. Calculated energy spectrum of **6** below 2 meV with $J=-1.18$ meV and $D=-0.031$ meV. The states are labelled with the dominant contribution to the wavefunctions in $|S,M_S\rangle$ notation. Vertical arrows indicate observed INS transitions with labels corresponding to the peak labels in Figure 10.

  

$|S,M_S\rangle$ notation. The vertical arrows represent the observed allowed transitions. Peak I corresponds to the transition within the zero-field split $S=3/2$ ground state and directly determines the value of $D_{Cr}$. Peaks II, III and V reflect transitions from the ground-state multiplet to the lowest lying $S=1/2$ and 5/2 multiplets. Peak IV consists of several transitions from the first excited $S=1/2$ state to close-lying higher $S=1/2$ and 3/2 states.

**Inelastic neutron scattering (INS) of 1 in a magnetic field**: Figure 13 shows the INS spectra obtained on FOCUS with $\lambda_i=5.5$ Å at approximately 40 mK after subtracting an analytical function to account for the background due to quasi-elastic diffuse scattering. At zero field a broad asymmetric

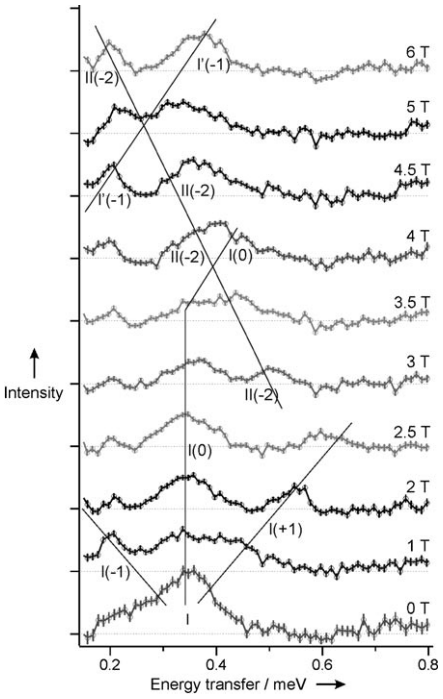


Figure 13. INS spectra of **1** obtained on FOCUS (PSI) with $\lambda_i=5.5$ Å at 40 mK in magnetic fields between 0 and 6 T. The solid lines are guides to the eye.

peak (peak I) at about 0.34(1) meV is observed, which corresponds to peak I in the IN5 data (Figure 8), and consists of the peaks Ia and Ib observed in the IRIS experiments (Figure 9; the resolution of the FOCUS experiment is too low to resolve the ZFS). With increasing field peak I is split into three components, I(−1), I(0), and I(+1). Between 2.5 and 3 T peak I(+1) disappears, peak I(0) has slightly moved upwards in energy and a new peak II(−2) at 0.50(3) meV appears. This peak moves further down with increasing field and at 3.5 and at 4 T is merged with peak I(0) into one broad peak. At 4.5 T the peak II(−2) becomes sharper again and is at lower energy, and another peak I′(−1) at 0.19(4) meV appears. Peak I′(−1) and peak II(−2) seem to cross between 5 and 6 T.

We fitted Gaussian curves to the observed peaks to get their positions with a single FWHM for all peaks at the same field.[40] Figure 14 shows a plot of the observed transition energies versus magnetic field, with the zero-field energy position taken from the IN5 data. The black solid line represents an isotropic calculation of the Zeeman splitting with $g=1.96$ of an $S=1$ and $S=2$ state set to the energies of 0.33 and 1.26 meV, respectively, obtained from the INS measurements. The calculations support the interpretation that we observe the Zeeman splitting of the lowest triplet and quintet state, and that in this field range the ground state changes from $S=0$ to $S=1$ at about 2.9 T.

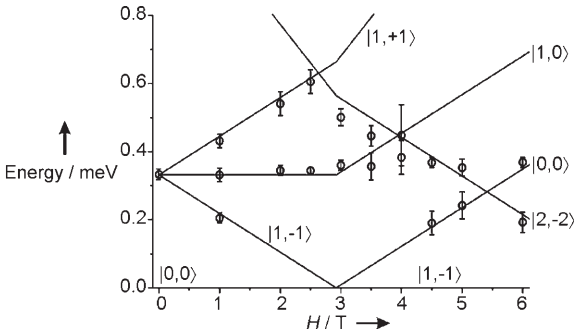


Figure 14. Field dependence of the measured energies for **1**. The black lines are the isotropically calculated Zeeman splitting of the first excited triplet and the first excited quintet state.

**EPR spectroscopy of 1, 2 and 6**: Compounds **1**, **2** and **6** give rich and temperature-dependent EPR spectra below 20 K. The spectra of **1** and **2** are very similar and therefore we only discuss our simulation of **2** in detail, with comparison with **1** drawn where appropriate. For **1** the simulation requires a range of $D$ values to simulate all features, and therefore the story is clearer for **2**.

For **2**, at both Q- and W-band, resonances are seen which can be assigned to $S=1$ and $S=2$ excited states (Figures 15 and 16). At low field a peak increases in intensity as the temperature is lowered, and this is assigned as the $\Delta ms=\pm 2$ transition of a spin triplet state. Most of the remaining

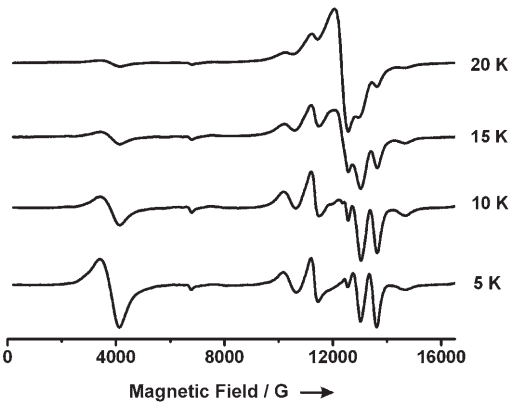


Figure 15. Variable-temperature EPR spectra of a microcrystalline sample of **2** recorded at Q-band (34 GHz) in eicosane.

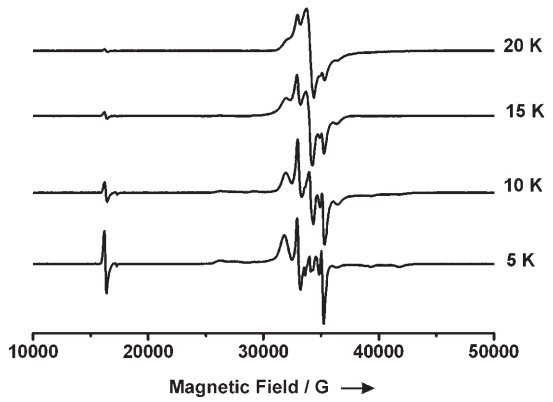


Figure 16. Variable-temperature EPR spectra of a microcrystalline sample of **2** recorded at W-band (94 GHz) in eicosane.

sharp features are due to a spin quintet state. Simulation of these two states separately followed by addition gives a good fit of the spectra (Figure 17). The simulation parameters used were: for the $S=1$ state, $g_x=1.995$, $g_y=1.980$, $g_z=1.970$, $D_{S=1}=-0.088$ meV, $\lambda=0.2$ ($E=-0.018$ meV), with a Gaussian linewidth ($W$) of 450 G; for the $S=2$ state, $g_x=g_y=1.976$, $g_z=1.972$, $D_{S=2}=0.017$ meV, $\lambda=-0.04$ ($E=-0.0007$ meV) and $B_4^0=3.4\times10^{-5}$ meV, with $W=180$ G. It was necessary to include the $B_4^0$ term to account for the intensity of the highest field feature due to the spin quintet.

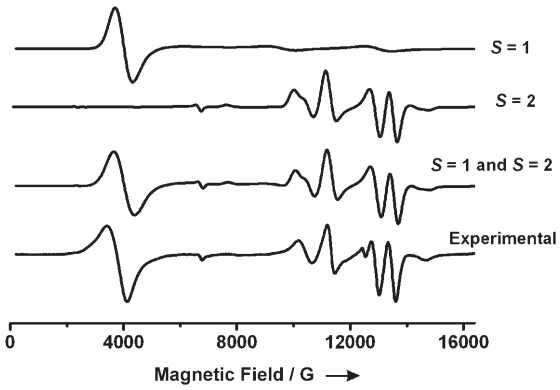


Figure 17. Analysis of the Q-band EPR spectrum of **2**. The simulation of the $S=1$ and $S=2$ spin states and the sum of the $S=1$ and $S=2$ states use parameters given in the text.

For **1** the lowest field feature, which is due to the $S=1$ state, is broadened. This implies a range of $D$ values for the $S=1$ state, and a simulation could be achieved by including two $S=1$ states (in a ratio of 3:1), with subtly different ZFS parameters. The major component has the parameters: $g_x=g_y=g_z=1.97$, $D_{S=1}=0.078$ meV, $E_{S=1}=-0.027$ meV, $W=300$ G; while the minor component has $g_x=g_y=g_z=1.97$, $D_{S=1}=0.084$ meV, $E_{S=1}=-0.026$ meV, $W=500$ G. The simulation also required for the $S=2$ state, $g_x=g_y=1.958$, $g_z=1.977$, $D_{S=2}=0.017$ meV, $E_{S=2}=0$, $B_4^0=4.0\times10^{-5}$ meV, $W=180$ G.

Compared with the INS studies of the double horseshoe **1**, it is clear that the ZFS for each spin state can be resolved by EPR spectroscopy, whereas by INS only bands involving the spin triplet show features due to ZFS. The $D$ values input to model the EPR spectra are for the individual spin states rather than the single-ion ZFS terms used for INS. To compare with the INS spectra, $D_{S=1}$ is half the energy gap between transitions Ia and Ib in Figure 10, which is measured by INS as 0.076 meV (see above). The value determined by EPR spectroscopy is therefore higher than that determined by INS.

For **6** the EPR spectra are less well-resolved (Figure 18). This is probably due to line-broadening due to dipolar exchange between the $S=3/2$ horseshoes in the dimeric structure. A sharp peak is seen for an $S=1/2$ excited state, with $g$ values of $g_{xy}=1.970$ and $g_z=1.916$. The resonances due to the $S=3/2$ ground state are broad, and can be simulated with: $g_x=1.94$, $g_y=1.89$, $g_z=1.96$, $D_{S=3/2}=-0.042$ meV, $E=0.010$ meV. To compare with the INS data, $D_{S=3/2}$ is half the energy gap between transitions II and III in Figure 10 and 11, that is, 0.09 meV. Here the agreement is better than for **2**.

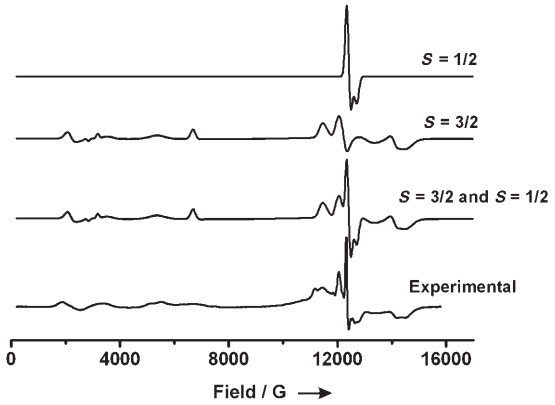


Figure 18. Experimental EPR spectrum for **6** at 5 K and Q-band (34 GHz) and simulation of the $S=3/2$ and $S=1/2$ spin states and the sum of the $S=3/2$ and $S=1/2$ states using parameters given in the text.

## Discussion

**Correlation of structure and magnetic behaviour**: The structures of the $\{Cr_6\}$ and $\{Cr_7\}$ horseshoes can be described as fragments of the homometallic wheel $[\{CrF(O_2CCMe_3)_2\}_8]$ (**7**) missing two or one $Cr^{III}$ centres, respectively.[14] There is very little change in the metric parameters between the horseshoes and the wheels, for example, Cr···Cr distances are all very similar at about 3.4 Å. There is a very subtle change in the average of the Cr···Cr···Cr angles, with this being 135° in **7** and 135.4° in **6**, but slightly smaller at near 133° in **1–5**. Cr-F-Cr bridging angles and Cr–F distances are also very similar for all seven compounds (Table 1). It is normally assumed that there is a correlation between structural

  

Table 1. Experimental data for X-ray diffraction studies of **1**–**6**.

| | **1** | **2** | **3** | **4** | **5** | **6** |
|---|---|---|---|---|---|---|
| formula | $C_{136}H_{284}Cr_{12}F_{22}N_6O_{44}$ | $C_{124}H_{264}Cr_{12}F_{22}N_6O_{46}$ | $C_{160}H_{320}Cr_{12}F_{22}N_6O_{42}$ | $C_{174}H_{348}Cr_{14}F_{24}N_6O_{56}$ | $C_{224}H_{466}Cr_{24}F_{44}N_{12}O_{90}$ | $C_{157}H_{315}Cr_{14}F_{24}N_6O_{49}$ |
| $M$ | 3749.70 | 3617.42 | 4042.22 | 4604.58 | 6852.08 | 4255.15 |
| crystal system | monoclinic | monoclinic | monoclinic | triclinic | triclinic | monoclinic |
| space group | $P2_1/n$ | $P2_1/a$ | $P2_1/c$ | $P\bar{1}$ | $P\bar{1}$ | $P2_1/n$ |
| $a$ [Å] | 19.7047(11) | 20.179(3) | 13.5117(5) | 16.5837(9) | 16.709(3) | 27.106(2) |
| $b$ [Å] | 25.7316(13) | 19.7482(11) | 19.9890(5) | 19.5298(11) | 23.500(5) | 32.551(3) |
| $c$ [Å] | 21.9000(11) | 26.749(3) | 42.9987(10) | 21.0610(9) | 25.771(5) | 27.3129(19) |
| $\alpha$ [°] | 90 | 90 | 90 | 84.139(4) | 78.41(3) | 90 |
| $\beta$ [°] | 111.545(5) | 110.523(13) | 93.429(3) | 81.387(4) | 76.04(3) | 93.509(6) |
| $\gamma$ [°] | 90 | 90 | 90 | 81.203(4) | 71.68(3) | 90 |
| $V$ [Å$^3$] | 10328.2(9) | 9983(2) | 11592.5(6) | 6643.0(6) | 9236(3) | 24054(3) |
| $T$ [K] | 100(2) | 100(2) | 100(2) | 100(2) | 100(2) | 100(2) |
| $Z$ | 2 | 2 | 2 | 1 | 1 | 4 |
| $\mu$ [mm$^{-1}$] | 0.685 | 0.707 | 0.614 | 0.625 | 0.631 | 0.683 |
| unique data | 10776 | 15931 | 12142 | 16130 | 21090 | 19021 |
| data with $F_o > 4\sigma(F_o)$ | 7245 | 7280 | 10670 | 8747 | 12547 | 10288 |
| $R1$, $wR2$[a] | 0.0957, 0.2810 | 0.0692, 0.2107 | 0.1717, 0.3643 | 0.0829, 0.2525 | 0.0943, 0.2743 | 0.0986, 0.3243 |

[a] $R1$ based on observed data, $wR2$ on all unique data.

parameters associated with the predominant superexchange path and magnetic exchange; if this is the case here the exchange interaction in the chains and rings should also be similar. This is not what we find. It is possible that there could be a correlation with other structural parameters, but given the complexity of the structures any such correlation is likely to be coincidental.

The INS spectra of **7** could be modelled with a single exchange coupling constant $J = -1.46$ meV.[41] Similar values for the Cr–Cr interaction have also been found for the heterometallic wheels with general formula $[R_2NH_2][Cr_7MF_8(O_2CCMe_3)_{16}]$ with $M = Ni^{II}$ ($J = -1.46$ meV), $Mn^{II}$ ($J = -1.43$ meV) and $Zn^{II}$ ($J = -1.43$ meV).[38] For **1** we found that the internal coupling constant, $J_B = -1.4$ meV; both the exchange path and the coordination geometries of the $Cr^{III}$ sites are identical to those in **7**, and hence the exchange interaction is very similar. However, the coupling at the ends of the horseshoe ($J_A$) is 20% smaller than $J_B$. Qualitatively, we could infer that the three terminal fluoride ions attached to each $Cr^{III}$ ion at the tips of the horseshoe withdraw electron density from the $Cr^{III}$ sites, and hence weaken these interactions. Curiously the INS spectra and magnetic data for **6** are best fitted with a single exchange parameter of $J = -1.18$ meV, that is, similar to $J_A$ rather than $J_B$. The single-ion ZFS parameters for **1**, $D = -0.028$ meV and $|E| = 0.005$ meV, and **6**, $D = -0.031$ meV, are in good agreement with the parameters found for **7** ($D = -0.029$ meV and $|E| = 0.004$ meV).[41] This agreement is perhaps coincidental; in **7** all $Cr^{III}$ sites are chemically equivalent, whereas in **1** and **6** the sites at the tips of the horseshoe have different coordination spheres to the $Cr^{III}$ sites within the horseshoe. Given that we have derived $D$ from the splitting of one excited state in **1** and the ground state in **6** it is possible that we have not been able to resolve different single-ion $D$ values.

Measurements of the equivalent parameters from fitting specific heat data,[42] in each case using only a single exchange parameter for all Cr···Cr interactions, give: for **1**, $J_{ex} = 1.190$ meV, $D_{Cr} = -0.026$ meV; for **6**, $J_{ex} = 1.172$ meV, $D_{Cr} = -0.026$ meV. These values are in good agreement with the INS values.

**Variations between structures**: While the arrangements of Cr and bridging atoms within the horseshoes is constant, and even very similar between $\{Cr_6\}$ and $\{Cr_7\}$ horseshoes, the arrangement of ammonium cations and hence the packing of horseshoes is very different within the six structures described here.

The first consideration is to examine why the change from $\{Cr_6\}$ to $\{Cr_7\}$ horseshoes when the secondary amine changes from having linear alkyl chains to branched. If we compare the four dimeric co-planar structures **1**–**3** and **6** there appears to be an interesting trend comparing where the nitrogen atom of the ammonium cation is relative to the Cr atoms of the horseshoe. This can be quantified if we set an edge to the horseshoe by imagining a line linking the outermost Cr centres, for example, Cr1 and Cr6 in Figure 1. For **2**, in which the cation is $Et_2NH_2$, the N atom is 0.97 Å from the edge of the horseshoe. Moving to **1**, in which we have $n Pr_2NH_2$ as cation, this same parameter is 0.84 Å and in **3**, with $n Bu_2NH_2$ the distance is down to 0.74 Å. Therefore as the alkyl group gets bigger, the cation moves towards the edge of the horseshoe. For **6**, in which there is a $\{Cr_7\}$ horseshoe, the cation is more contained within the anionic complex—averaging 1.28 Å from the "edge" defined by linking the outermost Cr centres. However, if we imagined the cation within a $\{Cr_6\}$ horseshoe, for example, by linking one tip chromium (Cr1) with one Cr adjacent to a tip (Cr6) the cation would be only 0.45 Å from the edge. The change from $\{Cr_6\}$ to $\{Cr_7\}$ therefore appears to be related to the need to encapsulate a single ammonium cation within the horseshoe's cavity.

This analysis does not explain the formation of a $\{Cr_7\}$ horseshoe in **4** in which the cation is $NEt_2H_2$. For **4** the N atom is 2.23 Å from the edge of the $\{Cr_7\}$ horseshoe, and

  

around 0.9 Å from the edge of a $\{Cr_6\}$ fragment, that is, it is in the same position with relation to six Cr ions in **4** as the same cation is in the $\{Cr_6\}$ horseshoe in **2**.

The tetrameric structure **5** is found for the smallest amine used, and it seems likely that the structure could not form if longer alkyl-chains were present on the cation. However, this does not explain why the use of $Me_2NH_2$ leads to the tetrameric structure rather than the dimeric structure. It does not seem any more hydrogen bonds are formed in **5** compared with the other structures.

Taken together these results suggest that the $\{Cr_x\}$ horseshoes could be used as hydrogen-bond acceptors to produce more complex arrays. This is an area worth exploring in the future.

**Energy spectrum, rotational bands and spin excitations in AFM chains**: The greatest understanding of the elementary excitations in molecular magnets comes from exact numerical diagonalisation studies. These have the drawback that they are limited to systems with a rather small number of spin centres, simply due to the computational power required to handle larger clusters. If insight into the physical nature of elementary excitations could be developed it may prove possible to develop theories which are more computationally inexpensive. In the following discussion we will assume that the Heisenberg term is dominant and we will ignore weaker effects, such as anisotropy, aiming to uncover generic features due to the Heisenberg interactions. The horseshoes studied in this work shall henceforth be described as "perfect" finite chains, with the Hamiltonian given in Equation (4).

$$\mathscr{H} = -J \sum_{j=1}^{N-1} \hat{\mathbf{S}}_j \hat{\mathbf{S}}_{j+1} \tag{4}$$

This is reasonable as the variation of the coupling constants and the ZFS terms are small perturbations ($N$ is the number of centres in the chain).

One general insight into Heisenberg spin clusters has emerged in the recent years, which we will call the L&E-band concept. It leads to a characteristic rotational-band structure in the energy spectrum, if plotted as function of $S$. The lowest energy level for every value of $S$ falls into an approximately parabolic band, called the L-band,[25–29] while the next-higher energy levels for every value of $S$ form a number of further approximately parabolic bands, which together are called the E-band (see Figure 19 for example).[25,26] Still higher energy levels then form a quasi-continuum of states. The L&E-band concept is further characterised by the selection rule that at low temperature almost all INS transitions with significant intensities should occur within the L- and E-bands, and should not involve the quasi-continuum.[25]

When this picture applies, the problem of determining magnetic properties is enormously simplified. First, the energies of the states within the L-band are proportional to $S(S+1)$, and hence characterised by one value $\Delta$, see Equation (5) in which the energy of the ground state was set to 0.

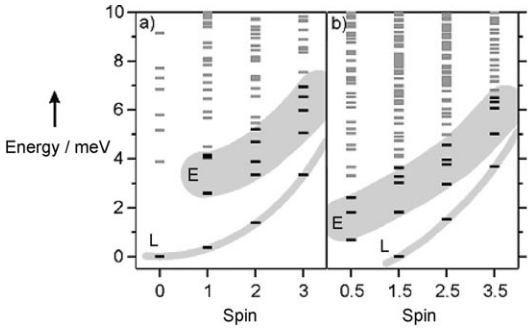


Figure 19. Calculated isotropic energy spectra below 10 meV vs. total spin $S$ for a) **1** for $S \leq 3$ and b) **6** for $S \leq 7/2$. The black states in the shaded regions constitute the L&E-bands. The grey states represent the quasi-continuum.

$$E(S) = (\Delta/2)S(S+1) \tag{5}$$

The thermodynamic properties (magnetisation, magnetic torque, specific heat) at low temperatures are largely determined by the L-band, and knowing $\Delta$ should be sufficient. Second, the energies of the states within the E-band are also proportional to $S(S+1)$, but shifted to higher energies, by increments $\varepsilon(q)$ given by Equation (6), in which $q$ is the number of the different branches in the E-band.

$$E(S,q) = (\Delta/2)S(S+1) + \varepsilon(q) \tag{6}$$

Furthermore, the above-mentioned selection rule applies, which guarantees that the INS spectrum at low temperature is governed by the L- and E-bands, that is, the few values $\Delta$ and $\varepsilon(q)$. Obtaining reasonable estimates for $\Delta$ turns out to be fairly easy; several approximates were suggested.[5,25–28,43] For $\varepsilon(q)$, the situation is much more involved; very recently spin-wave theory (SWT) was suggested.[25,30,44]

The L&E-band structure is currently believed to emerge for systems with a "classical" spin structure.[25–27,45,46] A system is "classical" if the Néel state (i.e., alternating "spin up"/"spin down") reflects well the spin structure in the ground state (here we limit ourselves to bipartite systems, such as even-numbered wheels or chains; for other cases the situation is far from clear[44]). The L-band states are then well approximated by wavefunctions of the form $|S_A,S_B,S,M_S\rangle$, in which $S_A$ and $S_B$ are the total spins of the two oppositely oriented sublattices (for **1**: $S_A = S_B = 3 \times S_j$; for **6**: $S_A = 4 \times S_j$, $S_B = 3 \times S_j$). Physically, the excitations within this band can be regarded as a combined rotation of the total spins of each sublattice, a so-called rotation of the Néel vector.[13,15,26,27] States in which $S_A$ or $S_B$ is reduced by 1 from their respective maximum value are called the E-band.[25] Physically, these states may be associated with (discrete) spin waves.[13,15,25,26]

The L&E-band concept seems to describe a larger class of Heisenberg spin clusters, and is generic in this sense. The

  

L-band is well documented for a number of molecular spin clusters, such as the AFM wheels,[5,10,15,25,43,47,48] the modified AFM wheels,[39,42,49] the [3×3] grids,[13,50,51] the $\{Mo_{72}Fe_{30}\}$ cage[52] and other clusters. Observing the E-band directly is possible only with INS, hence evidence is scarce; it is well documented for the AFM wheels,[15] and the Mn-[3×3] grid;[50] for $\{Mo_{72}Fe_{30}\}$ evidence is also strong.[52,53] In addition, the SMM $Mn_{12}$ seems to be characterised by a classical spin structure.[54]

The linkage between L&E-band picture and "classical" spin structure suggests the use of SWTs, which are semi-classical theories.[26] However, by construction SWTs are not appropriate for small-spin clusters; they all start with the key assumption of a long-range-ordered ground state, which in small clusters is never obeyed. Efforts have been made to overcome this deficiency, leading to the so-called finite-size or modified SWTs, but the problem remains. Hence, although successful in the case of extended systems, applying SWTs to small clusters is questionable, and requires very careful comparative studies. However, SWTs can be easily applied to rather big systems, when it would be impossible to treat the problem by matrix diagonalisation. Furthermore, in principle they can provide values for the parameters $\Delta$ and $\varepsilon(q)$ of Equations (5) and (6).

Considering the above context, whether the L&E-band concept could be applied to finite chains has been examined. Examining the INS spectra for **1** we find that transitions I, II and III correspond to transitions within the L-band, while transitions V and VI are transitions from the L-band to the E-band (see Figures 9 and 14). Similarly for **6** the transitions II/III and IV are L-band transitions (transition II/III is split into II and III due to ZFS), and transition V is a transition from the L-band to the E-band. Hence, our studies 1) extend the (short) list of systems in which spin waves (=E-band) have been observed experimentally, and 2) confirm the L&E-band picture also for AFM finite chains. The latter point is also demonstrated by the calculated energy spectra shown in Figure 14.

We have previously discussed the spin-wave excitations V and VI in **1** (see Figure 11),[30] and we could show that the spin waves in finite chains are best described as standing waves due to the open boundaries, compared to the periodic boundary conditions in wheels, in which the spin waves are running waves. In both the hexanuclear wheel and chain, four different AFM spin-wave excitations are present, but in the wheel they are essentially degenerate and give rise to only one INS transition, while in the chain they are split into two sets each of two quasi-degenerate states, hence giving rise to two transitions in the INS spectrum (transitions V and VI in **1**). The splitting of otherwise degenerate spin-wave states is a direct effect of the open-boundary conditions. This has a neat analogy in chemistry, which actually can be found in any chemistry textbook; it will be discussed next.

**Analogy of Hückel molecular orbitals in benzene and hexatriene and spin waves in hexanuclear wheels and chains**: The analogy of the splitting of the spin-wave bands in **1** is observed also in the molecule 1,3,5-hexatriene, in comparison to benzene. Figure 20 shows the energy spectra of benzene and hexatriene, in the Hückel approximation. The case of benzene is described in any textbook. The Hückel method results in diagonalising a Hamiltonian matrix of the form displayed in Figure 20, with matrix elements $\alpha$ and $\beta$. In accord with the cyclic symmetry, the states have the symmetry labels $a_{2u}$, $e_{1g}$, $e_{2u}$, and $b_{2g}$ in symmetry group $D_{6h}$, or $q=0$, $\pm1/3\pi$, $\pm2/3\pi$, $\pi$ in symmetry group $C_6$, respectively ($q$ is sort of a wave vector, which for $q\neq0$, $\pi$ represents left and right running waves of electronic charge density). Going to hexatriene, the one missing bond breaks the cyclic symmetry, giving rise to open boundaries and a reduction of the symmetry to $C_{2v}$, and symmetry labels $a_2$ and $b_1$. The resultant Hamiltonian matrix is shown in Figure 20 (in textbooks often the similar case of butadiene is discussed). The main effect of the reduced symmetry is of course to split the otherwise degenerate states, that is, the $e_{1g}$ and $e_{2u}$ states. The new states may be obtained by treating the missing bond in first-order perturbation theory, which yields that the $e_{1g}$ states split into $|2/3\pi\rangle \pm |-2/3\pi\rangle$ and the $e_{2u}$ states into $|1/3\pi\rangle \pm |-1/3\pi\rangle$. These are the linear and antilinear combinations of left ($q<0$) and right ($q>0$) running waves, that is, standing waves. Despite the large splitting, the first-order treatment is actually rather good; the first-order result for the splitting is only 17% too small. In a very similar way do the otherwise degenerate spin-wave excitations split in AFM chains.[30]

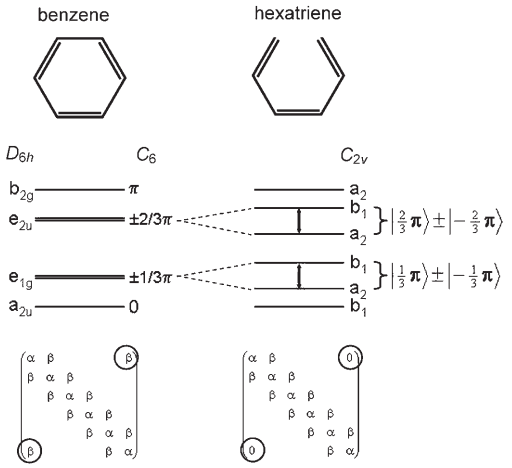


Figure 20. The molecular structure of benzene and hexatriene and their respective energy levels as calculated by diagonalising the Hückel matrices (bottom).

The analogy between the Hückel molecular orbitals and the spin waves in Heisenberg clusters would be perfect for a spin cluster with ferromagnetic exchange interactions. For AFM spin clusters the situation is subtler because of reasons too involved to be outlined here, hence resulting in a somewhat different energy spectrum (for AFM wheels, the four states with $q=\pm1/3\pi$, $\pm2/3\pi$ are essentially degenerate),

  

but the mechanism of the splitting of the spin-wave bands is correctly captured.

## Conclusion

The results here show that both hexa- and heptanuclear chromium chains can be made straightforwardly. The crystallisation of these chains appears to be dependent on the ammonium cation present, which influences where we see mono-, di- or trimeric assemblies of horseshoes in the crystal. We have determined the exchange couplings and the single-ion anisotropy of representative examples of $\{Cr_6\}$ and $\{Cr_7\}$ and observed the Zeeman splitting of the first excited states.

## Experimental Section

The reagents were from Aldrich and used as received. Complexes were prepared in Erlenmeyer Teflon® FEP flasks (capacity 125 mL) supplied by Fisher.

**$[\{[nPr_2NH_2]_3[Cr_6F_{11}(O_2CCMe_3)_{10}]\}_2]$ (1)**: Pivalic acid (16.0 g, 157 mmol), di-*n*-propylamine (2.25 g, 22 mmol) and $CrF_3{\cdot}4H_2O$ (5.0 g, 28 mmol) were stirred together at 140 °C for 15 h in an open Teflon flask. After cooling to room temperature, acetone (50 mL) was added to the solid and it was stirred for 5 h. The solid was collected by filtration, washed with acetone and dried in air. This product was extracted with diethyl ether (75 mL). The obtained extract was filtered, diluted with MeCN (30 mL) and stirred for 30 min. The resulting green microcrystalline product was collected by filtration, washed with a large quantity of MeCN, then thoroughly washed with acetone, and dried in air. Yield 6.1 g (71.4 %); elemental analysis calculated (%) for $C_{136}H_{280}Cr_{12}F_{22}N_6O_{42}$: Cr 16.80, C 43.99, H 7.60, N 2.26; found: Cr 16.87, C 43.92, H 7.39, N 2.25. Suitable crystals for an X-ray structure study were obtained from a solution of pentane/acetone (2:1) by slow evaporation of the solvents at room temperature over 3 d. Compound **1** was recrystallised from pentane/acetone prior to the sample being used for INS studies.

**$[\{[Et_2NH_2]_3[Cr_6F_{11}(O_2CCMe_3)_{10}]\}_2]$ (2)**: Compound **2** was obtained by the same procedure as for **1**, but using diethylamine in place of di-*n*-propylamine. Yield 6.4 g (78.40 %); elemental analysis calculated (%) for $C_{124}H_{256}Cr_{12}F_{22}N_6O_{42}$ : Cr 17.60, C 42.01, H 7.28, N 2.37; found: Cr 17.32, C 42.27, H 7.52, N 2.42. X-ray quality single crystals were obtained from a solution of THF/$CH_3CN$ (1:1) at room temperature after 2 d.

**$[\{[nBu_2NH_2]_3[Cr_6F_{11}(O_2CCMe_3)_{10}]\}_2]$ (3)**: Compound **3** was obtained by the same procedure as for **1**, but using di-*n*-butylamine instead of diethylamine. However an additional extraction of the initial solid was performed. The first extraction was performed with diethyl ether ($2\times75$ mL) and the resulting solution was evaporated to dryness to give a green product that was washed with acetone and dried in air to yield 2.3 g of powder. Elemental analysis calculated (%) for $C_{148}H_{300}Cr_{12}F_{22}N_6O_{40}$: Cr 16.22, C 46.22, H 7.86, N 2.19; found: Cr 16.04, C 45.88, H 8.10, N 2.07. Suitable crystals for an X-ray structure study (reported here) were obtained from a solution of hexane/toluene by slow evaporation of the solvent at room temperature.

A second extraction of the original precipitate was performed using a mixture of 2:1 THF/toluene (150 mL) at 50–60 °C. Concentration of this extract by evaporation gave 3.2 g of crystalline product, including crystals suitable for X-ray study, which confirmed the same structure as found for the product from $Et_2O$ extract. Elemental analysis calculated (%) for $C_{148}H_{300}Cr_{12}F_{22}N_6O_{40}$: Cr 16.22, C 46.22, H 7.86, N 2.19; found (for the sample dried in vacuo): Cr 15.89, C 45.83, H 8.42, N 2.01. Overall yield: 5.5 g (62 %).

**$[\{[Me_2NH_2]_3[Cr_6F_{11}(O_2CCMe_3)_{10}]{\cdot}2.5H_2O\}_4]$ (5)**: Pivalic acid (16.0 g, 157 mmol), dimethylammonium dimethylcarbamate (1.34 g, 10 mmol, as source of the dimethylammonium cation) and $CrF_3{\cdot}4H_2O$ (5.0 g, 28 mmol) were stirred together at 140 °C for 30 h. After cooling to room temperature, diethyl ether (20 mL) and acetone (50 mL) were added and the solution was stirred for 5 h. Then it was filtered and the filtrate diluted with MeCN (70 mL) and stirred for 3 d. The precipitate that formed during this time was collected by filtration, washed with a large amount of MeCN and then extracted into $Et_2O$ (20 mL). The extract was diluted with MeCN (30 mL) and stirred for 30 min. The green solid that precipitated was collected by filtration, washed with a large amount of MeCN and with acetone (10 mL), and dried in air. Yield 0.32 g (2.0 %); elemental analysis calculated (%) for $C_{224}H_{476}Cr_{24}F_{44}N_{12}O_{90}$ : Cr 18.19, C 39.21, H 6.99, N 2.45; found: Cr 17.71, C 38.73, H 7.12, N 2.27. Suitable crystals for X-ray studies were obtained from a solution of ethyl acetate/acetonitrile (1:1) at room temperature after 1 d.

**$[\{[iPr_2NH_2]_3[Cr_7F_{12}(O_2CCMe_3)_{12}]\}_2]$ (6)**: Pivalic acid (16.0 g, 157 mmol), diisopropylamine (2.0 g, 22 mmol) and $CrF_3{\cdot}4H_2O$ (5.0 g, 28 mmol) were stirred together at 140 °C for 18 h. The green viscous mass which resulted was heated at 100 °C for 5 h under a $N_2$ flow to remove unreacted pivalic acid. After cooling to room temperature, acetone (50 mL) was added to the solid and it was stirred for 5 h. The remaining precipitate was collected by filtration and washed with a large amount of acetone and dried in air. This product was extracted into diethyl ether (75 mL), the solvent was evaporated and the residue washed with acetone and dried on air. Yield 1.7 g (20.20 %); elemental analysis calculated (%) for $C_{156}H_{316}Cr_{14}F_{24}N_6O_{50}$ : Cr 17.09, C 43.98, H 7.48, N 1.97; found: Cr 16.83, C 44.31, H 7.71, N 2.13. X-ray quality single crystals could be obtained by crystallisation from pentane/acetone, $Et_2O$/acetone or toluene/$CH_3CN$. Here we report the structure of the crystals from pentane/acetone, which is also the sample used for INS studies. Elemental analysis calculated (%) for $C_{156}H_{316}Cr_{14}F_{24}N_6O_{50}$ : Cr 17.09, C 43.98, H 7.48, N 1.97, F 10.70; found: Cr 17.15, C 43.99, H 7.44, N 1.86, F 10.81.

**X-ray studies**: Data were collected on Bruker SMART CCD diffractometer ($Mo_{K\alpha}$, $\lambda = 0.71073$ Å except **2** for which $\lambda = 0.6892$ Å was used). In all cases the selected crystals were mounted on the tip of a glass pin using Paratone-N oil and placed in the cold flow produced with an Oxford Cryocooling device.[55] Complete hemispheres of data were collected using $\omega$-scans (0.3°, 30 seconds/frame). Integrated intensities were obtained with SAINT+[56] and they were corrected for absorption using SADABS.[56] Structure solution and refinement was performed with the SHELX-package.[56] The structures were solved by direct methods and completed by iterative cycles of $\Delta F$ syntheses and full-matrix least-squares refinement against $F$.

CCDC-676802 (**1**), -676803 (**2**), -676804 (**3**), -676805 (**4**), -676806 (**5**) and -676807 (**6**) contain the supplementary crystallographic data for this paper. These data can be obtained free of charge from The Cambridge Crystallographic Data Centre via www.ccdc.cam.ac.uk/data_request/cif.

**Magnetic measurements**: Magnetic measurements were performed in the temperature range 1.8–300 K, by using a Quantum Design MPMS-XL SQUID magnetometer equipped with a 7 T magnet. The diamagnetic corrections for the compounds were estimated using Pascal's constants, and magnetic data were corrected for diamagnetic contributions of the sample holder.

**Inelastic neutron scattering (INS) measurements**: The following instruments were used for the INS experiments: the direct geometry time-of-flight (TOF) spectrometer IN5 at the Institut Laue-Langevin (ILL), Grenoble (France), the inverted geometry TOF spectrometer IRIS at the ISIS facility, CCLRC Rutherford Appleton Laboratory, Didcot (UK), and the direct TOF spectrometer FOCUS at the Paul Scherrer Institut (PSI), Villigen (Switzerland).

For the INS experiment on IN5, approximately 4 g of non-deuterated polycrystalline sample were filled into an aluminium cylinder with outer diameter 14 mm and height 55 mm in a helium atmosphere. Measurements were performed with an initial neutron wavelength of $\lambda_i = 3.0$ Å at 1.7 K and 3.8 Å at 1.6, 9.5 and 20 K. The elastic resolution {full-width-half-maximum (FWHM)} was 0.4 and 0.17 meV, respectively. The experimental temperatures were achieved with a $^4$He-Orange ILL cryostat. For

  

the TOF to energy conversion and the data reduction the ILL program INX was used.

For the IRIS experiment approximately 2 g of non-deuterated polycrystalline sample were sealed under helium in a hollow aluminium cylinder with 24 mm outer diameter, 1 mm sample space, and 50 mm height. The final neutron wavelength of $\lambda_f = 6.66$ Å was selected with the (002) reflection of a pyrolytic graphite analyser, yielding a resolution at the elastic line of 17.5 μeV. A $^4$He-Orange cryostat was employed to reach the experimental temperatures of 1.5 and 10 K. A spectrum of vanadium metal was used to correct for detector efficiency and spurious instrumental peaks.

The FOCUS experiment was performed on approximately 4 g of non-deuterated polycrystalline sample, sealed under helium in a copper cylinder of 14 mm outer diameter and 50 mm height. The initial neutron wavelength was $\lambda_i = 5.5$ Å. An Oxford Instruments Kelvinox $^3$He/$^4$He dilution insert was used inside a 9 T Oxford Instruments cryomagnet. A base temperature of 40 mK was achieved, and a maximum field of 6 T could be applied vertically. Due to the smaller window of the cryomagnet only the middle of three detector banks could be used.

**EPR measurements**: EPR spectra were measured on powders at 34 GHz (Q-band) on a Bruker ESP 300E spectrometer and 90 GHz (W-band) on a Bruker E690 CW spectrometer. EPR simulations were performed using the program EPR-SIM.[57]

## Acknowledgements

This work was funded by the EPSRC (UK), the Swiss National Science Foundation (NFP 47), The Leverhulme Trust and the European Union (TMR Quemolna MRTN-CT-2003-504880 and NE MAGMANet 515767-2). We thank Prof. Høgni Weihe for use of EPR simulation software.

[1] D. Gatteschi, R. Sessoli, *J. Magn. Magn. Mater.* **2004**, *272–276*, 1030–1036.
[2] D. Gatteschi, R. Sessoli, *Angew. Chem.* **2003**, *115*, 278–309; *Angew. Chem. Int. Ed.* **2003**, *42*, 268–297.
[3] G. Aromi, E. K. Brechin, *Struct. Bonding (Berlin)* **2006**, *122*, 1–68.
[4] R. Bircher, G. Chaboussant, C. Dobe, H. U. Güdel, S. T. Ochsenbein, A. Sieber, O. Waldmann, *Adv. Funct. Mater.* **2006**, *16*, 209–220.
[5] K. L. Taft, C. D. Delfs, G. C. Papaefthymiou, S. Foner, D. Gatteschi, S. J. Lippard, *J. Am. Chem. Soc.* **1994**, *116*, 823–833.
[6] Q. Chen, S. Liu, J. Zubieta, *Inorg. Chem.* **1989**, *28*, 4434–4435.
[7] V. L. Pecoraro, A. J. Stemmler, B. R. Gibney, J. J. Bodwin, H. Wang, J. W. Kampf and A. Barwinski, *Prog. Inorg. Chem.* **1997**, *45*, 83–177.
[8] R. W. Saalfrank, I. Bernt, E. Uller, F. Hampel, *Angew. Chem.* **1997**, *109*, 2596–2599; *Angew. Chem. Int. Ed. Engl.* **1997**, *36*, 2482–2485.
[9] M. Affronte, S. Carretta, G. A. Timco, R. E. P. Winpenny, *Chem. Commun.* **2007**, 1789–1797.
[10] J. van Slageren, R. Sessoli, D. Gatteschi, A. A. Smith, M. Helliwell, R. E. P. Winpenny, A. Cornia, A.-L. Barra, A. G. M. Jansen, E. Rentschler, G. A. Timco, *Chem. Eur. J.* **2002**, *8*, 277–285.
[11] R. H. Laye, M. Murrie, S. Ochsenbein, A. R. Bell, S. J. Teat, J. Raftery, H. U. Güdel, E. J. L. McInnes, *Chem. Eur. J.* **2003**, *9*, 6215–6220.
[12] D. M. Low, G. Rajamaran, M. Helliwell, G. A. Timco, J. van Slageren, R. Sessoli, S. Ochsenbein, R. Bircher, C. Dobe, O. Waldmann, H. U. Güdel, M. A. Adams, E. Ruiz, S. Alvarez, E. J. L. McInnes, *Chem. Eur. J.* **2006**, *12*, 1385–1396.
[13] O. Waldmann, *Coord. Chem. Rev.* **2005**, *249*, 2550–2566.
[14] E. J. L. McInnes, S. Piligkos, G. A. Timco, R. E. P. Winpenny, *Coord. Chem. Rev.* **2005**, *249*, 2577–2590.
[15] O. Waldmann, T. Guidi, S. Carretta, C. Mondelli, A. L. Dearden, *Phys. Rev. Lett.* **2003**, *91*, 237202/1–237202/4.
[16] O. Waldmann, C. Dobe, H. Mutka, A. Furrer, H. U. Güdel, *Phys. Rev. Lett.* **2005**, *95*, 057202/1–057202/4.
[17] S. Carretta, P. Santini, G. Amoretti, T. Guidi, J. R. D. Copley, Y. Qiu, R. Caciuffo, G. Timco and R. E. P. Winpenny, *Phys. Rev. Lett.* **2007**, *98*, 167401/1–167401/4.
[18] F. Meier, J. Levy, D. Loss, *Phys. Rev. Lett.* **2003**, *90*, 047901/1–047901/4.
[19] F. Troiani, A. Ghirri, M. Affronte, S. Carretta, P. Santini, G. Amoretti, S. Piligkos, G. Timco and R. E. P. Winpenny, *Phys. Rev. Lett.* **2005**, *94*, 207208/1–207208/4.
[20] A. Ardavan, O. Rival, J. J. L. Morton, S. J. Blundell, A. M. Tyryshkin, G. A. Timco, R. E. P. Winpenny, *Phys. Rev. Lett.* 2007, ***98***, 057201/1–057201/4.
[21] S.-M. Peng, C.-C. Wang, Y.-L. Jang, Y.-H. Chen, F.-Y. Li, C.-Y. Mou, M.-K. Leung, *J. Magn. Magn. Mater.* **2000**, *209*, 80–83.
[22] R. H. Ismayilov, W.-Z. Wang, R.-R. Wang, C.-Y. Yeh, G.-H. Lee, S.-M. Peng, *Chem. Commun.* **2007**, 1121–1123.
[23] W.-Z. Wang, R. H. Ismayilov, G.-H. Lee, I. P.-C. Liu, C.-Y. Yeh, S.-M. Peng, *Dalton Trans.* **2007**, 830–839.
[24] F. K. Larsen, J. Overgaard, S. Parsons, E. Rentschler, A. A. Smith, G. A. Timco, R. E. P. Winpenny, *Angew. Chem.* **2003**, *115*, 6160–6163; *Angew. Chem. Int. Ed.* **2003**, *42*, 5978–5981.
[25] O. Waldmann, *Phys. Rev. B* **2002**, *65*, 024424/1–024424/13.
[26] P. W. Anderson, *Phys. Rev.* **1952**, *86*, 694–701.
[27] B. Bernu, C. Lhuillier, L. Pierre, *Phys. Rev. Lett.* **1992**, *69*, 2590–2593.
[28] J. Schnack, M. Luban, *Phys. Rev. B* **2000**, *63*, 014418/1–014418/7.
[29] L. Engelhardt, M. Luban, *Phys. Rev. B* **2006**, *73*, 054430/1–054430/9.
[30] S. T. Ochsenbein, O. Waldmann, A. Sieber, G. Carver, R. Bircher, H. U. Güdel, R. S. G. Davies, G. A. Timco, R. E. P. Winpenny, H. Mutka, F. Fernandez-Alonso, *Europhys. Lett.* **2007**, *79*, 17003/1–17003/6.
[31] O. Cador, D. Gatteschi, R. Sessoli, F. K. Larsen, J. Overgaard, A.-L. Barra, S. J. Teat, G. A. Timco, R. E. P. Winpenny, *Angew. Chem.* **2004**, *116*, 5308–5312; *Angew. Chem. Int. Ed.* **2004**, *43*, 5196–5200.
[32] M. Shanmugam, L. P. Englehardt, F. K. Larsen, M. Luban, C. A. Muryn, E. J. L. McInnes, J. Overgaard, E. Rentschler, G. A. Timco, R. E. P. Winpenny, *Chem. Eur. J.* **2006**, *12*, 8267–8275.
[33] L. P. Engelhardt, C. A. Muryn, R. G. Pritchard, G. A. Timco, F. Tuna, R. E. P. Winpenny, *Angew. Chem.* **2008**, *120*, 938–941.
[34] $BF = 1 + \{\exp(E/kT)\}^{-1}$.
[35] R. Basler, C. Boskovic, G. Chaboussant, H. U. Güdel, M. Murrie, S. T. Ochsenbein, A. Sieber, *ChemPhysChem* **2003**, *4*, 910–926.
[36] O. Waldmann, *Phys. Rev. B* **2003**, *68*, 174406/1–174406/8.
[37] O. Waldmann, H. U. Güdel, *Phys. Rev. B* **2005**, *72*, 094422/1–094422/17.
[38] A. Furrer, H. U. Güdel, *Phys. Rev. Lett.* **1977**, *39*, 657–660.
[39] R. Caciuffo, T. Guidi, S. Carretta, P. Santini, G. Amoretti, C. Mondelli, G. Timco, R. E. P. Winpenny, *Phys. Rev. B* **2005**, *71*, 174407/1–174407/8.
[40] The small sharp feature at ≈0.2 meV observed between 2 and 4 T could not be fit with the same width as the other peaks. Fitting it independently yielded a FWHM below 50 μeV, while the FWHM is 70 μeV for the elastic line, and around 90 μeV for the other peaks. We thus conclude that it is an artefact of the background subtraction or spurious instrumental feature.
[41] S. Carretta, J. van Slageren, T. Guidi, E. Liviotti, C. Mondelli, D. Rovai, A. Cornia, A. L. Dearden, F. Carsughi, M. Affronte, C. D. Frost, R. E. P. Winpenny, D. Gatteschi, G. Amoretti, R. Caciuffo, *Phys. Rev. B* **2003**, *67*, 094405/1–094405/8.
[42] A. Ghirri, A. Candini, M. Evangelisti, M. Affronte, S. Carretta, P. Santini, G. Amoretti, R. S. G. Davies, G. Timco, R. E. P. Winpenny, *Phys. Rev. B* **2007**, *76*, 214405/1–214405/8.
[43] A. Caneschi, A. Cornia, A. C. Fabretti, S. Foner, D. Gatteschi, R. Grandi, L. Schenetti, *Chem. Eur. J.* **1996**, *2*, 1379–1387.
[44] O. Waldmann, *Phys. Rev. B* **2007**, *75*, 012415/1–012415/4.
[45] O. Waldmann, *Europhys. Lett.* **2002**, *57*, 618–619.
[46] H. J. Schmidt, J. Schnack, M. Luban, *Europhys. Lett.* **2002**, *57*, 620–621.

  

[47] A. Cornia, M. Affronte, A. G. M. Jansen, G. L. Abbati, D. Gatteschi, *Angew. Chem.* **1999**, *111*, 2409–2411; *Angew. Chem. Int. Ed.* **1999**, *38*, 2264–2266; A. Cornia, A. G. M. Jansen, M. Affronte, *Phys. Rev. B* **1999**, *60*, 12177–12183.
[48] O. Waldmann, J. Schülein, R. Koch, P. Müller, I. Bernt, R. W. Saalfrank, H. P. Andres, H. U. Güdel, P. Allenspach, *Inorg. Chem.* **1999**, *38*, 5879–5886; O. Waldmann, R. Koch, S. Schromm, J. Schülein, P. Müller, I. Bernt, R. W. Saalfrank, F. Hampel, E. Balthes, *Inorg. Chem.* **2001**, *40*, 2986–2995.
[49] S. Carretta, P. Santini, G. Amoretti, M. Affronte, A. Ghirri, I. Sheikin, S. Piligkos, G. Timco, R. E. P. Winpenny, *Phys. Rev. B* **2005**, *72*, 060403/1–060403/8.
[50] O. Waldmann, S. Carretta, P. Santini, R. Koch, A. G. M. Jansen, G. Amoretti, R. Caciuffo, L. Zhao, L. K. Thompson, *Phys. Rev. Lett.* **2004**, *92*, 096403/1–096403/4; T. Guidi, S. Carretta, P. Santini, E. Liviotti, N. Magnani, C. Mondelli, O. Waldmann, L. K. Thompson, L. Zhao, C. D. Frost, G. Amoretti, R. Caciuffo, *Phys. Rev. B* **2004**, *69*, 104432/1–104432/8.
[51] O. Waldmann, H. U. Güdel, T. L. Kelly, L. K. Thompson, *Inorg. Chem.* **2006**, *45*, 3295–3300.
[52] J. Schnack, M. Luban, R. Modler, *Europhys. Lett.* **2001**, *56*, 863–869.
[53] O. Cépas, T. Ziman, *Prog. Theor. Phys. Suppl.* **2005**, *159*, 280–291.
[54] G. Chaboussant, A. Sieber, S. Ochsenbein, H. U. Güdel, M. Murrie, A. Honecker, N. Fukushima, B. Normand, *Phys. Rev. B* **2004**, *70*, 104422/1–104422/16.
[55] J. Cosier, A. M. Glazer, *J. Appl. Crystallogr.* **1986**, *19*, 105–107.
[56] SHELX-PC Package, Bruker Analytical X-ray Systems, Madison, WI, **1998**.
[57] J. Glerup, H. Weihe, *Acta Chem. Scand.* **1991**, *45*, 444.

Received: February 5, 2008
Published online: May 9, 2008

  